

Escaping the maze: a statistical sub-grid model for cloud-scale density structures in the interstellar medium

Tobias Buck^{1*}, Bogdan Corobean¹, Philipp Girichidis^{2,1}, Christoph Pfrommer¹, Keri Dixon^{3,4}

¹Leibniz-Institut für Astrophysik Potsdam (AIP), An der Sternwarte 16, D-14482 Potsdam, Germany


²Universität Heidelberg, Zentrum für Astronomie, Institut für Theoretische Astrophysik (ITA), Albert-Ueberle-Str. 2, D-69120 Heidelberg, Germany

³New York University Abu Dhabi, PO Box 129188, Abu Dhabi, United Arab Emirates

⁴Center for Astro, Particle and Planetary Physics (CAP³), New York University Abu Dhabi

Accepted XXXX . Received XXXX; in original form XXXX

ABSTRACT

The interstellar medium (ISM) inside galactic disks is a highly structured, multiphase medium but state-of-the-art cosmological simulations of the formation of galactic disks usually lack the resolution to properly resolve those structures. Small scale density structures can have an important effect on several physical aspects of the interstellar medium such as the fraction of cold, the 4π sky distribution of dense gas or the amount of radiation and momentum leakage from cloud embedded sources. Here we derive a *statistical model* for small scale ISM density structures using the *gas clumping factor*. The model we present is explicitly tailored to be applicable as a sub-grid prescription for coarse-grained simulations of the ISM which lack the resolution to directly model small scale structures. Applying our model to calculate the number of optically thick sight-lines of interstellar gas clouds, usually referred to as the covering fraction, shows that small scale density structures lead to significant differences at fixed physical ISM density. Our model predicts that gas clumping results in covering fractions ranging from as low as 10% up to 100% at typical ISM densities. All data and example code is publicly available at GitHub .

Key words: methods: analytical - methods: statistical - methods: numerical - galaxies: formation - galaxies: structure - ISM: structure

1 INTRODUCTION

The interstellar medium (ISM) of galaxies is a highly structured, multi-component distribution of gas. The densest regions inside the ISM are giant molecular clouds (GMCs) with sizes of a few tens of parsecs. Those regions of gas and dust undergo local gravitational collapse, forming dense cores in which new stars are born. The structure and morphology of GMCs is shaped by large scale supersonic turbulence leading to the formation of density enhancements such as filaments, clumps, and cores.

A statistical representation of the influence of supersonic turbulence on the structure of molecular clouds is given by the probability distribution function (PDF) of the mass density. For isothermal, supersonic turbulent gas a lognormal density distribution is expected (e.g. Vazquez-Semadeni 1994; Nordlund & Padoan 1999; Ostriker et al. 2001; Klessen 2000; Padoan & Nordlund 2002; Krumholz & McKee 2005;

Wada & Norman 2007; Hennebelle & Chabrier 2008; Konstandin et al. 2012; Girichidis et al. 2014). Recent observations by Kainulainen et al. (2009) showed further that also the column density PDFs of GMCs exhibit a lognormal distribution.

In general, star formation is expected to occur in the coldest and densest parts of the ISM dominated by molecular gas (e.g. Kennicutt & Evans 2012). Successive mechanical and radiative energy input from young massive stars will disperse and ionize the dense gas damping further star formation, although the effect of self-shielding can diminish radiation feedback, and thus may enable further star formation. In fact, the existence of H α emission around young star forming regions is a prominent signature of rapidly operating feedback processes in and around those star-forming regions (e.g. Kreckel et al. 2018).

Accurately modeling the star formation–feedback cycle is a key prerequisite in shaping galactic properties both on the scales of the ISM (e.g. Girichidis et al. 2016; Semenov et al. 2017; Semenov et al. 2021; Gutcke et al. 2021) as well

* E-mail:tbuck@aip.de

as the formation of galaxies in the cosmological context (e.g. Governato et al. 2010; Brook et al. 2012; Stinson et al. 2013; Agertz et al. 2013; Agertz & Kravtsov 2015, 2016; Hopkins et al. 2018; Buck et al. 2021; Applebaum et al. 2020, 2021). In the past few years important progress has been made in modeling star formation, feedback (e.g. Marinacci et al. 2019; Emerick et al. 2019; Benincasa et al. 2020; Smith et al. 2020), radiation hydrodynamics (e.g. Kannan et al. 2014, 2016, 2020; Emerick et al. 2018; Obreja et al. 2019), non-thermal feedback processes (e.g. Pfrommer et al. 2017; Buck et al. 2020b) as well as the chemistry of the ISM (e.g. Robertson & Kravtsov 2008; Gnedin & Kravtsov 2010, 2011; Hopkins et al. 2011; Christensen et al. 2012; Buck et al. 2021). Despite the great advancements in numerical resolution and the successes of the models, there is still great uncertainty in the relevant physical processes and their specific numerical implementation as subgrid recipes (see e.g. Somerville & Davé 2015; Naab & Ostriker 2017; Vogelsberger et al. 2020, for recent reviews).

Implementing physical processes below the resolution limit of the simulation poses substantial challenges for current galaxy formation models (e.g. Keller et al. 2019; Munshi et al. 2019; Genel et al. 2019; Buck et al. 2019). Depending on the implementation of the subgrid models either careful calibration against observations or fine tuning of parameter combinations are required. Often, this procedure results in somewhat disconnecting the subgrid model from the resolved scales of the simulation in the sense that (i) the calibration is not obtained from coarse-graining small-scale simulations and (ii) only few models do not require re-tuning parameters if run at different numerical resolution.

One way to improve upon the current state-of-the-art is to develop new subgrid-scale models which derive statistical properties of the gas from high-resolution ISM simulations and apply those to large-scale (cosmological) simulations in which those scales are not directly resolved, this establishing a connection with the resolved scales. Here we develop such a statistical model for the density distribution or porosity of the ISM on scales of a few ten parsecs. Our newly derived model is ideally suited to estimate the fraction of dense gas below the resolution limit (see section 2.2 Domínguez-Tenreiro et al. 2014) or to calculate H_2 fractions (e.g. Gnedin et al. 2009; Christensen et al. 2012) or to calculate the surface mass density distribution of GMCs from their average density alone. The model is able to self-consistently predict the 4π column density distribution around stars and the corresponding covering fraction (the number of optically thin sight-lines) of ISM clouds. It is therefore well suited to be coupled with e.g. radiation-hydrodynamic schemes to calculate the (UV) photon escape fractions for radiation sources from e.g. their birth clouds (see also Mao et al. 2020; Bianco et al. 2021, for a similar approach to subgrid modelling IGM clumping).

In §2 we discuss the probability distribution function of the ISM and explore in particular the log-normal density distribution and its summary statistics. In §3 we look at the cloud scale column density distribution and derive the covering fraction as a function of average density. In §4 we validate and compare our model to simulations from the SILCC (Walch et al. 2015) project and in section §5 we turn to discuss the application of the model to simultaneously describe the star formation from cold, dense gas as well as

the energetic and radiative feedback process in simulations. We finish in §7 with a summary of our results.

2 THE PROBABILITY DISTRIBUTION FUNCTION OF THE ISM

In this chapter we will derive a connection between the gas density clumping factor and the variance of the gas density PDF. For this, we define the *volume-weighted* gas density PDF, $f_V(\rho)$, and similarly the *mass-weighted* density PDF. We can relate $f_V(\rho)$ to $f_M(\rho)$, using the fact that $f_M \propto dM/d\rho$ and $f_V \propto dV/d\rho$ (e.g. Ostriker et al. 2001). From this we find $f_M(\rho) \propto \rho f_V(\rho)$ (see e.g. section 3.3.1 of Li et al. 2003).

2.1 Log-normal Density PDFs

The density PDF in the ISM varies between the different regimes and the spatial scales. In low-density regions, in which self-gravity is negligible and turbulence dominates, the density PDF can be approximated by a log-normal distribution. In dense regions that are gravitationally collapsing, the PDF develops a high-density power-law tail (e.g. Klessen 2000; Slyz et al. 2005; Federrath & Klessen 2012; Girichidis et al. 2014). On scales of GMCs and above, the density PDF $f(\rho)$ is in agreement with a single log-normal probability distribution function (LN-PDF e.g. Berkhuijsen & Fletcher 2008, 2015):

$$f_V(\rho)d\rho = \frac{1}{\sqrt{2\pi}\sigma} \exp\left[-\frac{\ln(\rho/\rho_0)^2}{2\sigma^2}\right] \frac{d\rho}{\rho}, \quad (1)$$

where ρ_0 is the characteristic density (or equivalently the median of the distribution) and σ is the width of that distribution. Noting that $\rho > 0$, the corresponding cumulative function for the log-normal density distribution is given by:

$$P(\rho \leq \rho_{\text{thr}}) = \frac{1}{2} \left(1 + \text{Erf} \left[\frac{\ln(\rho_{\text{thr}}/\rho_0)}{\sqrt{2}\sigma} \right] \right). \quad (2)$$

From Eq. (1) we can derive the volume-averaged density $\langle \rho \rangle_V$ of the gas following a log-normal distribution:

$$\langle \rho \rangle_V = \int_0^\infty \rho f_V(\rho) d\rho = \rho_0 e^{\sigma^2/2}. \quad (3)$$

Correspondingly, the mass-weighted density is given by

$$\langle \rho \rangle_M = \int_0^\infty \rho f_M(\rho) d\rho = \int_0^\infty C \rho^2 f_V(\rho) d\rho \quad (4)$$

where we have used the fact that $f_M(\rho) = C \rho f_V(\rho)$. C can easily be determined by the requirement that the PDF is normalised, i.e. $\int_0^\infty f_M(\rho) d\rho = \int_0^\infty C \rho f_V(\rho) d\rho = 1$ which gives

$$C^{-1} = \rho_0 e^{\sigma^2/2} \quad (5)$$

by comparing to eq. (3). Thus, the mass-weighted density evaluates to

$$\langle \rho \rangle_M = \rho_0 e^{3\sigma^2/2} \quad (6)$$

These relations define a simple form for the dispersion σ of the LN-PDF:

$$\sigma^2 = \ln \left(\frac{\langle \rho \rangle_M}{\langle \rho \rangle_V} \right) \quad (7)$$

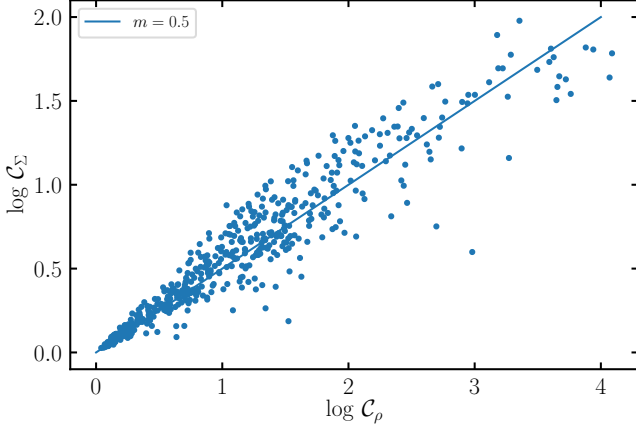


Figure 1. Three-dimensional clumping factor, C_ρ vs. projected clumping factor, C_Σ . We find that the projected clumping factor follows from the three-dimensional clumping factor as $C_\Sigma = \sqrt{C_\rho}$.



Which we can also rewrite using ρ_0 ,

$$\sigma^2 = 2 \ln \left(\frac{\langle \rho \rangle_V}{\rho_0} \right) \quad (8)$$

$$= \frac{2}{3} \ln \left(\frac{\langle \rho \rangle_M}{\rho_0} \right) \quad (9)$$

Under the assumption of nearly constant characteristic density ρ_0 , Equations (8) and (9) imply that the dispersion σ is proportional to the total mass of the system.

The above equations show that, for a stable, uniform system, i.e. $\langle \rho \rangle_V = \rho_0$, σ will be zero. On the other hand, if $\langle \rho \rangle_V \rightarrow \infty$, $\sigma \rightarrow \infty$, which in fact resembles a dynamically unstable system. Therefore, we expect that in a globally stable, inhomogeneous system σ will take on numbers in an appropriate range.

In order to establish a connection between $\langle \rho \rangle_V$ and $\langle \rho \rangle_M$, we define the clumping factor for the density C_ρ as their ratio:

$$C_\rho \equiv \frac{\langle \rho^2 \rangle_V}{\langle \rho \rangle_V^2} = \frac{\langle \rho \rangle_M}{\langle \rho \rangle_V} \quad (10)$$

Combining this definition with Eq. (7) and the fact that the median of the log-normal is given by $\text{MED}(\rho) = \rho_0$ Eqs. (8) and (9) state σ as the ratio of mean over median.

2.2 Cloud-scale column density distribution

It is well established that inter-stellar gas clouds are not entities of uniform density but highly structured objects (e.g. Heyer & Dame 2015) with dense clumps and filaments embedded into lower density gas. Therefore, for a given sphere of size, R , the column density on its surface will be highly structured as well. That means in a structured medium there will be a difference between the surface mass density measured over an area A (like e.g. the whole surface of a sphere) which is equal to the *area weighted surface mass density*,

$$\langle \Sigma \rangle_A \equiv \frac{\int_A \Sigma dA}{\int_A dA}, \quad (11)$$

and the true surface mass density at which most of the mass is found, the *mass weighted surface mass density* $\langle \Sigma \rangle_M$.

$$\langle \Sigma \rangle_M \equiv \frac{\int \Sigma dM}{\int dM} = \frac{\int_A \Sigma^2 dA}{\int_A \Sigma dA}. \quad (12)$$

For a uniform medium the two quantities $\langle \Sigma \rangle_M$ and $\langle \Sigma \rangle_A$ will be the same. In a highly clumped medium where most of the mass resides in small, high column density regions spread over large, low column density areas the two quantities will differ significantly. In order to establish a connection between those two quantities, we define the clumping factor for the column density C_Σ as their ratio:

$$C_\Sigma \equiv \frac{\langle \Sigma^2 \rangle_A}{\langle \Sigma \rangle_A^2} = \frac{\langle \Sigma \rangle_M}{\langle \Sigma \rangle_A} \quad (13)$$

(see also equ. 3 in Leroy et al. 2013). This definition is equivalent to the definition of the clumping factor via the volume density ρ as given in Eq. (10).

For a uniform density distribution where by definition $C_\rho = 1$ we expect the surface mass density distribution to be a delta distribution around the average area weighted surface mass density. The more the medium is clumped, the broader the distribution gets since we will find some areas on the sphere which are more dense due to clumping and others which (for mass conservation reasons) are under-dense.

Figure 1 shows the relation between C_ρ and C_Σ . Similar to Eckert et al. (2015, Appendix A) we find a square-root dependence between the three-dimensional clumping factor and the column-density clumping factor. This relation will be used later to write the covering fraction in terms of the three-dimensional density of the ISM.

Numerical studies of ISM turbulence (e.g. Federrath et al. 2010) have further established a relation between clumping factor, C_ρ , with the turbulence parameter b and the Mach number, \mathcal{M} :

$$C_\rho = 1 + b^2 \mathcal{M}^2. \quad (14)$$

And this can further be related to the column density fluctuations under specific assumptions (see e.g. Burkhart & Lazarian 2012).

We can further derive a connection between the volume weighted density and the area weighted surface density as follows:

$$\begin{aligned} \langle \rho \rangle_V &= \frac{\int_V \rho dV}{\int_V dV} = \frac{\int_V \rho dx dA}{\int_V dV} \\ &= \frac{\int_A \Sigma dA}{\int_V dV} \frac{\int_A dA}{\int_A dA} = \frac{\int_A \Sigma dA}{\int_A dA} \frac{\int_A dA}{\int_V dV} \\ &= \langle \Sigma \rangle_A \frac{3}{R} \end{aligned} \quad (15)$$

where in the last step we have used the definition of the area weighted surface density from eq. (11) and the fact that we integrate over a sphere of radius R for which $\int_V dV = \frac{4\pi}{3} R^3$ and $\int_A dA = 4\pi R^2$.

This finally enables us to equate the area weighted surface density as a function of the mean (mass-weighted) density, $\bar{\rho}$, of a finite patch of the ISM. For this we use that $f_M \propto dM/d\rho$ which enables us to write the total mass of the system as $M = \int_0^\infty dM \propto \int_0^\infty \rho f_M(\rho) d\rho$ which gives:

$$\bar{\rho} = \frac{M}{V} = \langle \rho \rangle_M = C_\rho \langle \rho \rangle_V \quad (16)$$

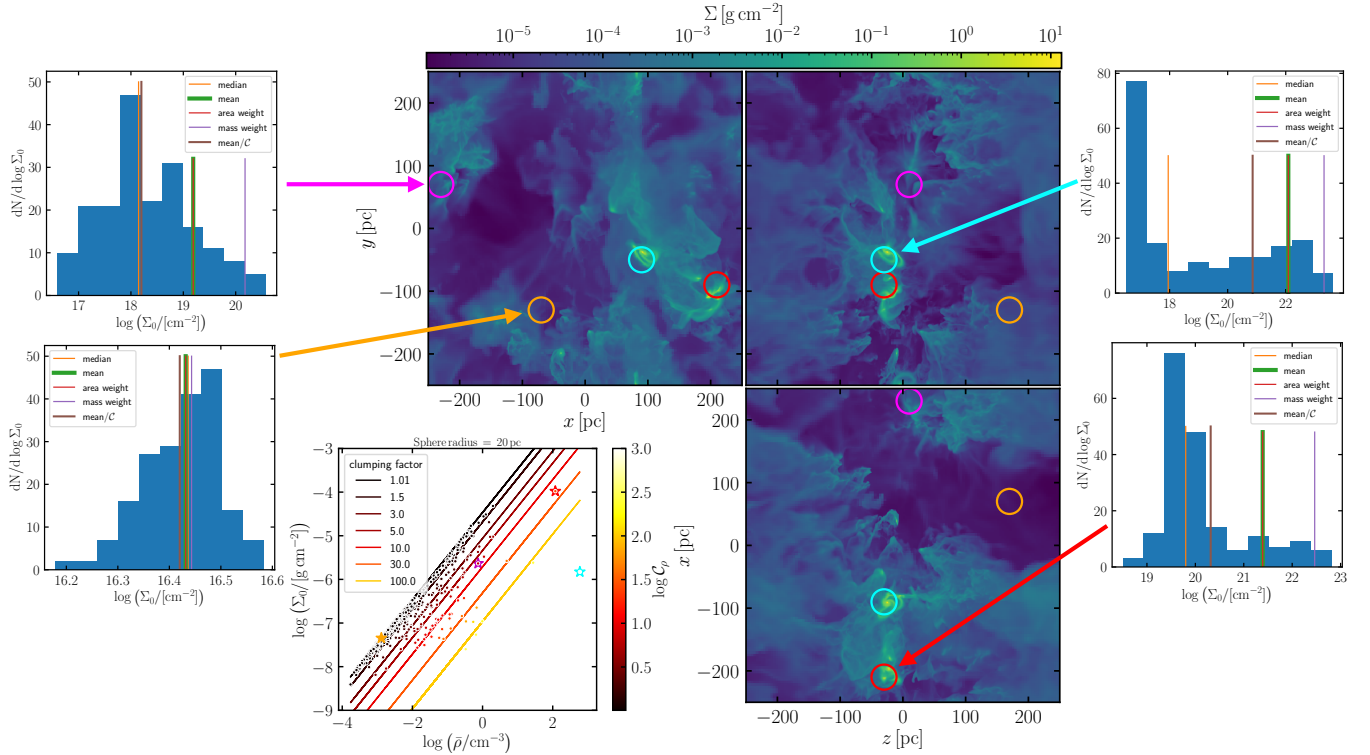



Figure 2. Illustration of the impact of the clumping factor on the column density distribution. The histograms show the column density distribution of four example spheres of radius $R = 20$ pc at different locations in the ISM as shown with colored circles in the surface density plot in the center panels. The two left histograms show low density more uniform environments while the two right histograms show high density, highly clumped environments. The lower left panel displays the relation between peak column density Σ_0 and average three dimensional density, $\bar{\rho}$, of all spheres with radius $R = 20$ pc shown with colored dots. Colored lines highlight the theoretical relation from Eq. (23). For both, the lines and the points, the color-coding gives the value of the clumping factor. 

where we have used the definition of the clumping factor in the last step.

Equation (16) implies that the average density in a given volume (defined as the mass divided by the volume) for a highly clumped medium is reduced by the clumping factor. This can intuitively be understood by the following example: Supposed all the mass M is clumped together in a tiny volume V_1 but we wish to calculate the density $\bar{\rho}$ on a larger volume V_2 . Then $\bar{\rho} = \frac{M}{V_2}$ is smaller compared to $\rho = \frac{M}{V_1}$. In fact, this is exactly what the clumping factor expresses. The difference between mass weighted and volume weighted density in a clumpy medium.

Therefore, eq. (16) enables a simple way to estimate gas density substructure based on average density. With this, sub-grid H_2 fractions can be estimated in a similar way as in (Gnedin et al. 2009; Lupi et al. 2018). However, the focus here is more on cloud scale column density.

We rewrite eq. (15) as a function the mean density of a given finite volume of the ISM as:

$$\langle \Sigma \rangle_A = \frac{R}{3C_p} \bar{\rho} \quad (17)$$

2.3 Covering fractions from column density distributions

For many astrophysical phenomena (especially the ones including sources and sinks) one of the most important quan-

ties is the distribution of column density values. Especially for processes including radiation the interesting property is the fraction of lines-of-sight, $N(\geq \delta)$, above a given threshold of mass surface density, δ , above which the radiation is completely absorbed. This fraction is often referred to as the covering fraction which we define as:

$$P(\Sigma \geq \delta) = \frac{N(\geq \delta)}{N_{\text{tot}}} \quad (18)$$

where N_{tot} refers to the total number of sight lines.

Under the simple assumption that the column density on the sphere surface is log-normally distributed the fraction of sight lines with column density values above a given threshold $\log \delta$, is mathematically given by the cumulative function of the log-normal distribution which is known as the error function (see also Elmegreen 2002; Wada & Norman 2007, for a similar argument). In fact, the fraction of regions with column density larger than a threshold $\ln \delta$ is given by:

$$P(\Sigma \geq \delta) = \frac{1}{2} \left(1 - \text{Erf} \left[\frac{\ln(\delta/\sigma)}{\sqrt{2}\sigma_{\ln \Sigma}} \right] \right) \quad (19)$$

for column densities following a log-normal distribution with characteristic surface density Σ_0 and width $\sigma_{\ln \Sigma}$.

In Section 2.1, we have seen that for a log-normal distribution the width $\sigma_{\log \Sigma}$ is related to the ratio of area weighted to mass weighted surface mass density (Eq. 7)

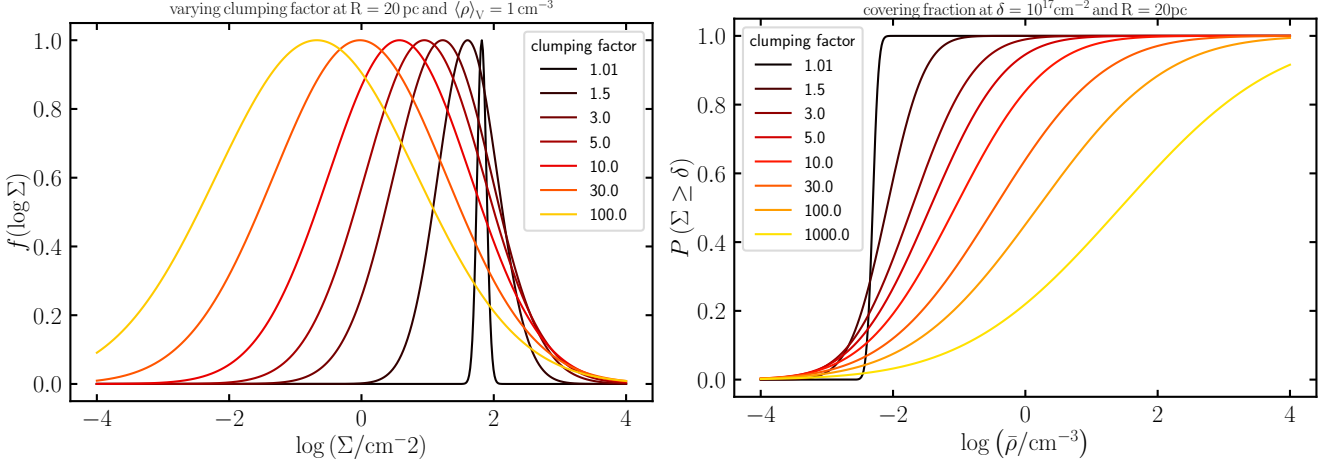


Figure 3. The left panel shows the column density distribution of a representative spherical patch of the ISM based on our analytical model. To exemplify the impact of ISM clumping on the width of the column density distribution we show results for different clumping factors. In the right panel we show the covering fraction as a function of ISM density as derived in Eq. (26). For this plot we have chosen a spherical region of 20 pc radius and a column density threshold of 10^{17} cm^{-2} chosen to roughly match the Lyman limit HI column density which is given by $N_{\text{HI}^{\text{thick}}} \sim 7.3 \times 10^{17} \text{ cm}^{-2}$. Again we exemplify the impact of ISM clumping by showing the results for different clumping factors. 📌

which exactly resembles our definition of the clumping factor in Eq. 13. Therefore, we rewrite $\sigma_{\ln \Sigma}$ in terms of the clumping factor (see also Gnedin et al. 2009; Lupi et al. 2018) as:

$$\sigma_{\ln \Sigma}^2 = \ln C_{\Sigma} \quad (20)$$

Similarly, the characteristic surface density is related to the area weighted density by:

$$\langle \Sigma \rangle_A = \Sigma_0 \exp(\sigma_{\ln \Sigma}^2/2) \quad (21)$$

which we will use to express Σ_0 in terms of the clumping factor C_{ρ} for the three-dimensional density and the average density inside the sphere $\bar{\rho}$ as derived in Eq. (17). This results in

$$\Sigma_0 = \frac{R}{3C_{\rho}} \bar{\rho} \exp\left(-\frac{\ln C_{\Sigma}}{2}\right). \quad (22)$$

It turns out now, there is no one-to-one relation between the clumping factor measured from the three-dimensional density field, C_{ρ} and the projected clumping factor measured from the surface density, C_{Σ} . Figure 1 shows the relation between projected clumping factor, C_{Σ} and the three-dimensional clumping factor, C_{ρ} which results in a square-root dependence of C_{Σ} on C_{ρ} (see also Appendix A of Eckert et al. 2015).

With this we can simplify Eq. (23) to:

$$\Sigma_0 = \frac{R}{3} \bar{\rho} C_{\rho}^{-5/4} \quad (23)$$

With the above two equations, Eq. (21) and Eq. (23), we are now fully equipped to derive a model for the column density distribution on the sphere which is solely dependent on the mean density inside the sphere, $\bar{\rho}$, and the clumpiness of the medium given by the value of C . And as such we are able to calculate the fraction of the 4π sphere around a point x in the ISM that is covered as a function of the average density inside the sphere of radius R . Combining Eqs. (21) and (23) and inserting them into Eq. (19) for the covering

fraction we arrive at our final equation:

$$P(\Sigma \geq \delta) = f(\bar{\rho}R, C_{\rho}, \delta) \quad (24)$$

$$= \frac{1}{2} \left(1 - \text{Erf} \left[\frac{\ln \left(\frac{3\delta}{R\bar{\rho}} C_{\rho}^{5/4} \right)}{\sqrt{2 \ln C}} \right] \right) \quad (25)$$

$$= \frac{1}{2} \left(1 - \text{Erf} \left[\frac{\ln \hat{\rho} - \hat{\mu}}{\sqrt{2} \hat{\sigma}} \right] \right) \quad (26)$$

In the last step we have rewritten our result for enhanced clarity in terms of an effective density, $\hat{\rho}$, an effective peak position, $\hat{\mu}$, and an effective width, $\hat{\sigma}$, defined as follows:

$$\hat{\rho} \equiv \frac{3\delta}{R\bar{\rho}}, \quad \hat{\mu} \equiv -\frac{5}{4} \ln C_{\rho}, \quad \hat{\sigma} \equiv \sqrt{\frac{\ln C_{\rho}}{2}}. \quad (27)$$

3 A STATISTICAL MODEL FOR SUB-GRID ISM CLUMPING AND CLOUD-SCALE COVERING FRACTIONS

The aim of this work is to derive a statistical model for the sub-grid structure of the ISM which can readily be applied to coarse resolution simulations such as cosmological simulations of the formation of Milky Way-like galaxies. Those simulations usually lack the spatial resolution to properly resolve the multi-phase nature of the ISM. In section 2 we have derived our theoretical model for the sub-grid clumping of the ISM and its effect on e.g. the covering fraction of (molecular) gas clouds. In order to gauge the performance of our model we compare it to state-of-the-art resolved ISM simulations from the SILCC project (Walch et al. 2015; Girichidis et al. 2016). For detailed descriptions of the numerical setup of the SILCC simulations and the physics models employed we refer the reader to these two references. The simulations used here are the higher resolution runs described in detail in Girichidis et al. (2018). For completeness, below we briefly describe the simulation and our procedure to extract cloud-scale data from it to compare to our model.

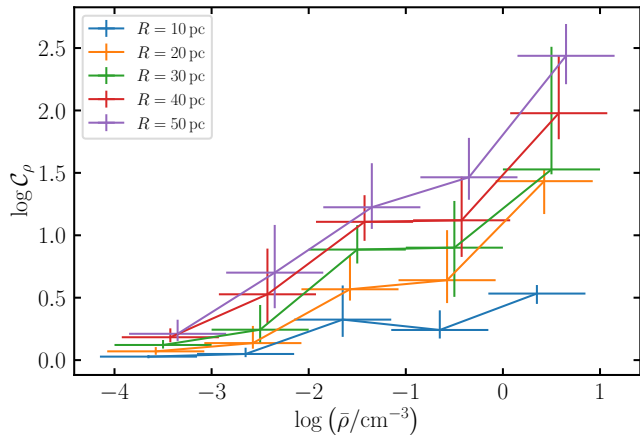


Figure 4. ISM clumping factor as a function of density for five different sphere radii as derived from the SILCC simulation. Horizontal error-bars show the bin width of 1 dex while vertical error-bars show the scatter around the median calculated as the 32nd and 68th percentile. For better visibility we have slightly offset the bins for different radii. 📍

3.1 SILCC simulations of the solar neighbourhood

The SILCC simulations correspond to a segment of a typical galactic disk at low redshift with solar neighborhood properties. The simulation domain for the higher resolution setups in Girichidis et al. (2018) focuses on the dense gas structures and covers is a $(500\text{pc})^3$ with a vertical stratification and the calculations are performed with the 3D magneto-hydrodynamic (MHD), adaptive mesh-refinement (AMR) code FLASH in version 4 (Fryxell et al. 2000; Dubey et al. 2008). In order to obtain an accurate picture of the ISM, the simulations include an external galactic potential, self-gravity, radiative heating and cooling, chemical evolution (which follows the formation of H_2 and CO molecules) with non-equilibrium abundances as in Nelson & Langer (1997), Glover & Mac Low (2007) and Micic et al. (2012), supernova feedback for both isolated and clustered SNe as well as magnetic fields (for a complete description of the simulation setup and physics implementation see Walch et al. 2015; Girichidis et al. 2016).

3.2 Data extraction using HEALPix

We statistically analyse different regions in the simulation domain by choosing randomly placed positions, x , and investigating spheres around that position with a fixed given radius, R . For each sphere we compute the average density as the main quantity of the analysis volume. To characterize the distribution of 4π column densities from the centres of the spheres to the radius, we make use of the HEALPix¹ (Gorski et al. 2005) tessellation of the unit sphere. HEALPix divides the surface of the unit sphere into quadrilateral, curvilinear pixels of varying shapes but equal area. The resolution depends on the N_{side} parameter, i.e. $N_{\text{pix}} = 12 \times N_{\text{side}}^2$, where N_{side} must be a power of two. For our analysis here we have chosen $N_{\text{side}} = 4$ corresponding to 192 cells on the

sphere surface. Tests with larger values for N_{side} show that our results are robust against changes in the HEALPix resolution.

We use the python implementation of the HEALPix algorithm from the healpy package (Zonca et al. 2019) in order to project the mass inside a spherical region of radius R onto its surface and evaluate the resulting distribution of column density pixel values. From the HEALPix tessellation we can further directly derive the surface density clumping factor, C_Σ as defined in Eq. (13) and the covering fraction as defined in Eq. (18) by counting the number of pixels with column density **above** a certain threshold value, δ , divided by the total number of pixels (in our case 192 pixels).

We perform our analysis for 5 different sphere radii ranging from 10 to 50 pc in increments of 10 pc representative of typical scales of gas clouds including their immediate vicinity, in which stellar feedback acts. These radii approximately corresponds to current resolutions of cosmological Milky Way simulations (e.g. Grand et al. 2017; Buck et al. 2020a; Applebaum et al. 2021; Agertz et al. 2021). For each radius we sample a total of 500 randomly chosen spheres from the simulations. A visual representation of typical sphere positions and their corresponding column density distribution is given in Figure 2. The four example spheres of radius $R = 20$ pc highlighted in this figure show the diversity of column density distributions resulting from different environments sampled from the simulation. This figure clearly shows that the average density is the main factor for differences in the column density distribution. The reason for this that higher density regions are statistically more structured than low density regions which exhibit a more uniform density distribution.

These findings are more quantitatively shown in Fig. 4 which uses the clumping factor defined in Eq. (10) to describe the structure of the ISM and which we discuss in detail in the next section.

3.3 ISM clumping for different environments

The only free parameter for the theoretical model derived in section 2 is the clumping factor, C_ρ , of the ISM. Choosing a value for C_ρ the sub-grid structure of a given patch of the ISM (the gas density distribution and the column density distribution and hence the covering fraction) is solely determined by the average ISM density, $\bar{\rho}$, of that region. Additionally, $\bar{\rho}$, the average density of a gas parcel, is exactly what coarse resolution simulations trace for all their resolution elements. Therefore, in order to establish a statistical model for the ISM which intersects self-consistently with coarse resolution simulations we need the (statistical) connection between the clumping factor and the average density.

Because of the above mentioned difficulties and to be flexible to adapt to new theoretical insights, we have established a phenomenological connection between the clumping factor and the ISM density from the SILCC simulations in Fig. 4. This figure shows the median clumping factor and its scatter (calculated as the 32nd and 68th percentile) as a function of ISM density and we show numerical values for each bin in Tab. 1.

The more uniform the ISM inside a given sphere, the closer to unity the clumping factor. The more substructure

¹ <http://healpix.sf.net>

Table 1. Clumping factor distributions as a function of density and sphere radius as derived from the SILCC simulations. For each radius we state the median, 32nd and the 68th percentile of the clumping factor for a range of ISM density bins.

$\log(\rho/\text{cm}^{-3})$	$(-4, -3)$	$(-3, -2)$	$(-2, -1)$	$(-1, 0)$	$(0, 1)$
R [pc]					
10	0.03 ^{0.04} _{0.01}	0.05 ^{0.1} _{0.02}	0.32 ^{0.6} _{0.19}	0.24 ^{0.4} _{0.17}	0.53 ^{0.6} _{0.45}
20	0.07 ^{0.1} _{0.04}	0.14 ^{0.27} _{0.09}	0.57 ^{0.84} _{0.43}	0.64 ^{1.04} _{0.46}	1.43 ^{1.52} _{1.17}
30	0.12 ^{0.16} _{0.09}	0.24 ^{0.44} _{0.14}	0.89 ^{1.08} _{0.77}	0.9 ^{1.28} _{0.51}	1.53 ^{2.51} _{1.49}
40	0.18 ^{0.25} _{0.14}	0.53 ^{0.89} _{0.3}	1.11 ^{1.32} _{0.96}	1.12 ^{1.47} _{0.83}	1.98 ^{2.44} _{1.77}
50	0.21 ^{0.32} _{0.15}	0.7 ^{1.08} _{0.42}	1.22 ^{1.58} _{1.05}	1.46 ^{1.78} _{1.28}	2.44 ^{2.69} _{2.21}

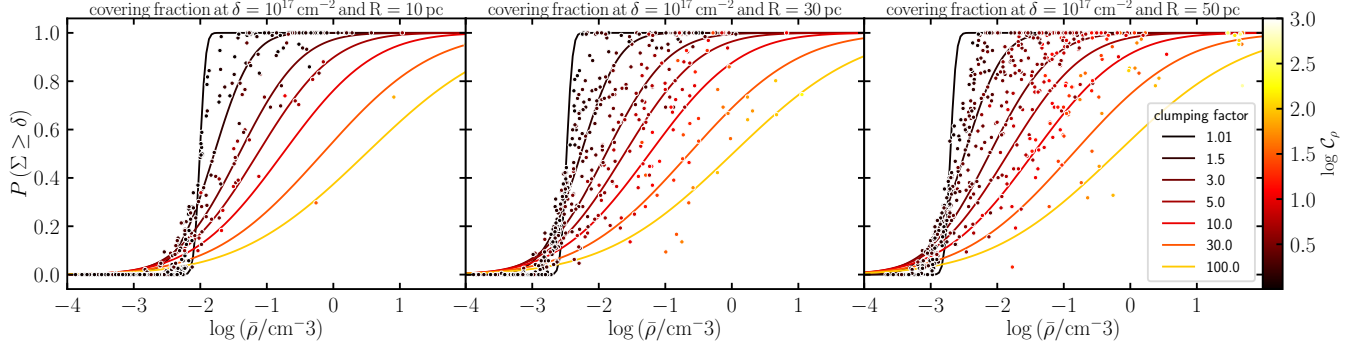



Figure 5. Comparison of the theoretical expectation (lines) for the covering fraction as a function of density with data from the SILCC simulations (colored dots) for fixed column density threshold of $\delta = 10^{17} \text{ cm}^{-2}$. The three different panels show increasing sphere radii from left to right as indicated by the panel's title. Again, the color-coding shows the clumping factor. 

we find, the larger the clumping factor becomes. Figure 4 clearly shows that for each radius probed in this work, the clumping factor increases with increasing ISM density, $\bar{\rho}$. For ISM densities below $\bar{\rho} \lesssim 10^{-2} \text{ cm}^{-3}$ the clumping factor is essentially equal to unity while for densities larger than this it rises quickly towards values around 10-100.

Furthermore, we see that there is a secondary correlation of the clumping factor with sphere radius. Larger sphere radii exhibit larger clumping factors independent of ISM density. This is simply due to the fact that the larger the region across which the density contrast is measured, the larger the possible fluctuations become.

Figure 4 enables us to statistically sample valid clumping factors as input to our model (see also section 2.3. III of Bianco et al. 2021, for a similar approach to sub-grid IGM clumping). With this approach we are then able to derive the sub-grid structure of the ISM gas and corresponding covering fractions as outlined in section 2.2.

3.4 Covering fractions of different environments

Finally, we gauge the validity of our model by comparing theoretical predictions for covering fractions to the results from the SILCC simulations. Figure 5 shows the covering fractions of patches of the ISM as a function of their average density, $\bar{\rho}$. From left to right, this figure shows the results for three different sphere radii as indicated by the top panel's title. Coloured lines show the results from our theoretical model for different clumping factors, C_ρ and coloured points show the covering fractions calculated for spherical regions of the ISM in the SILCC simulations. For both, the theoretical lines and the points the colour-coding shows the

clumping factor, C_ρ . For the 5 values of sphere radii probed in this work the correspondence between the model and the data is reasonably good and data points of a given clumping factor, C_ρ follow nicely the theoretically predicted curves of the same clumping factor, C_ρ .

3.5 Connecting covering fractions with photon escape fractions

Photons in the ISM escape through low density channels and there exist a clear correlation between e.g. Lyman continuum radiation and HI column density (e.g. Kakiichi & Gronke 2019). Figure 8 of Kakiichi & Gronke (2019) shows how the escape fraction of Lyman continuum radiation depends on the covering fraction in radiation hydrodynamical simulations. Their analysis reveals a near linear dependence of escape fractions on covering fractions with slopes of ~ 0.4 and ~ 0.6 depending on velocity dispersion. Combining our model for the covering fraction of ISM gas clouds with their results for the dependence of escape fractions on covering fractions it is straight forward to derive Lyman continuum or Lyman- α escape fractions for gas clouds in the ISM.

4 APPLICATIONS

4.1 Cold, dense gas and star formation

One common approximation in sub-resolution modelling of star formation is the introduction of a star formation efficiency parameter, ϵ_* , that measures the star formation rate per unit gas mass. For our purpose, ϵ_* measures the fraction of (gas) mass of the simulation resolution element con-

verted into stars in a given timestep. Since stars form from self-gravitating and collapsing gas clouds, this is simply the amount of gas above a given threshold density $\rho_{\text{crit}}/\rho_0$.

Equation (10) in combination with Eq. (2) allows us to equate the fraction of dense gas as a function of ρ_{crit} and clumping factor C_ρ :

$$P(\log \rho \geq \rho_{\text{crit}}) = \frac{1}{2} \left(1 - \text{Erf} \left[\frac{\log(\rho_{\text{crit}}/\rho_0)}{\sqrt{2 \ln C_\rho}} \right] \right) \equiv \epsilon_\star \quad (28)$$

For suitable choices of $\rho_{\text{crit}}/\rho_0$ and appropriate clumping factors C_ρ , either via eq. (14) or via sampling following Fig. 4 this equation immediately states the star formation efficiency ϵ_\star (see also section 2.2 of Lupi et al. 2018, for a similar approach to model the star formation efficiency).

4.2 Boosting of stellar winds and SNe

The expansion of spherical shock fronts such as supernova explosions or stellar wind bubbles strongly depends on the ambient medium (e.g. Kim & Ostriker 2015; Steinwandel et al. 2020; Gutcke et al. 2021; Lancaster et al. 2021a). Higher density ambient media damp the expansion of those bubbles. Or vice-versa, in lower density environment, SN explosions and stellar wind bubbles develop larger radial momentum. Especially, Haid et al. (2016) have shown in their figure 12 and equation 32 how the momentum of a single supernova exploding in a turbulent medium gets boosted compared to a uniform medium of the same average density (see also Fig. 17 of Lancaster et al. 2021b, for the retained stellar cluster wind energy in turbulent gas clouds). Thus, another application of our model is the calculation of the *effective* momentum input arising from clustered SN explosions or cluster winds in a non-uniform, turbulent medium.

The logic here is as follows: For a broader PDF, the density variations become larger and as such, the expanding blast wave encounters more low density regions. Those are subject to less radiative cooling and allow for a higher momentum injection. Similar to the calculation of the covering fraction in eq. (26), we can thus define a threshold surface mass density, δ_{FB} , above which the injected supernova or stellar wind energy will cause only little effect. Therefore, our model will self-consistently result in a coupling efficiency for feedback energy.

A reasonable choice for δ_{FB} can be derived by requiring the feedback energy, E_{FB} , in a given healpix cone to accelerate a column of gas of mass M_{cone} to velocities above $\sigma_{\text{GMC}} \sim 10$ km/s, the typical velocity dispersion of a GMC. With this the limiting column density becomes:

$$E_{\text{FB}} = \frac{1}{2} M_{\text{cone}} \sigma_{\text{GMC}}^2 = \frac{1}{2} \Sigma_{\text{cone}} A_{\text{cone}} \sigma_{\text{GMC}}^2 \quad (29)$$

In the last step we have used the fact that the mass in a given cone can be written in terms of the surface mass density in that cone, Σ_{cone} , times its area, $A_{\text{cone}} = (4\pi/N_{\text{cone}})R^2$. This results in the following threshold surface mass density when we replace $E_{\text{FB}} = E_{\text{tot}}/N_{\text{cone}}$:

$$\delta_{\text{FB}} = \frac{2E_{\text{tot}}}{\sigma_{\text{GMC}}^2 4\pi R^2} \quad (30)$$

Thus, replacing δ in eq. (26) will directly result in a density dependent efficiency parameter for the injection of feedback energy into the ISM.

5 DISCUSSION AND CONCLUSION

We set out to theoretically derive a model for the density structure of the interstellar medium with special emphasis on the applicability of the model as a sub-grid prescription of density structures in coarse-grained cosmological simulations.

Starting from the simple assumption that most gas in the ISM follows a log-normal density distribution we derive the column density distribution of spherically symmetric clouds as a function of average gas density. We explicitly incorporate the small-scale gas clumping into our model using the standard definition of gas clumping factor, C_ρ , as given by Eq. (10). Under the assumption of a log-normal density pdf the clumping factor directly relates to the width of the log-normal pdf, σ .

Our final result for the covering fraction as a function of ISM density is given by eq. (26). In our model, the covering fraction follows an error function (the cumulative function of the log-normal) whose centroid, μ , and width, σ , are modified by the amount of gas clumping characterized by, C_ρ . Thus, the only free input parameter to our model is the ISM clumping factor which depends on the physics on cloud scales. Using small scale ISM simulations this connection can statistically be established. Here, we have used parts of the SILCC simulations to derive how C_ρ behaves as a function of density (see Fig. 4).

While the assumption of a log-normal density PDF for the ISM gives reasonable results when compared to the SILCC simulations (see Fig. 5) this assumption might in fact be too simplistic as previous results have shown (e.g. Alves et al. 2017; Khullar et al. 2021). With the framework presented here, it is straight forward to replace the log-normal assumption and re-derive the equations for more complicated density PDFs. Similarly, the connection between gas clumping and density will depend on the exact physics modelled, e.g. it is well established that in idealized simulations there is a strong dependence of gas clumping on the Mach number (see Eq. 14).

However, when more physics such as cooling and feedback are considered, the dependence of gas clumping might become more complicated. With the approach chosen here of empirically deriving the gas clumping from small scale simulations the modelling procedure can easily adapt to new insights from more advanced simulations without changing the model. At the same time, this approach makes it easy to implement the model into coarse-grained simulations and to sample realistic gas clumping factors at runtime.

We summarize the main ingredients of our model as follows:

- There is a linear relation between the average density and the median column density of spherically symmetric gas clouds in the ISM. In particular, the median column density of clouds and the width of the distribution depends on the clumping factor as shown in Fig. 3.
- As expected, the ISM density and column density PDFs take the shape of a log-normal. For the PDFs, the characteristic densities and widths, σ , are functions of the gas clumping factor, C_ρ .
- Defining the covering fraction of a gas cloud as the ratio of number of sight lines above a given density threshold to the total number of sight lines, we derive a functional rela-

tion between covering fraction and cloud density in Eq. (26). Our model follows an error function which reflects our assumption of a log-normal density PDF. The only free parameter of this model is the gas clumping factor at a given cloud density.

- We have characterized the relation between gas clumping and average ISM density using a set of simulations from the SILCC simulations (Fig. 4). We find a strong correlation between average density and clumping factor. This empirically derived relation enables sampling valid values of C_ρ to model sub-grid density structures in coarse-grained simulations such as cosmological models for the Milky Way.

- Gas clumping has a strong effect on the covering fraction at fixed ISM density (see Fig. 5). Our model predicts that at a given density the cloud covering fractions can vary between ~ 0.1 up to 1. This implies that for a given spatial scale and average ISM density a gas cloud might be completely opaque to radiation emitted from its center or contrary let all the radiation freely escape, solely dependent on the amount of gas clumping inside the cloud.

- Combining our prescription with results from radiative transfer simulations to connect the covering fraction with the escape fraction of photons from gas clouds the model can readily be used to estimate photon escape fractions from embedded sources in the ISM.

DATA AVAILABILITY

SILCC simulations are publicly available at <http://silcc.mpa-garching.mpg.de>. A Jupyter notebook containing all plotting routines and data files can be found here: https://github.com/TobiBu/ISM_subgrid_clumping.git

ACKNOWLEDGMENTS

The authors like to thank Aura Obreja and Sven Buder for valuable comments to an earlier version of this draft which helped to improve clarity and readability of the manuscript. This research made use of the MATPLOTLIB (Hunter 2007), SCIPY (Jones et al. 01) and NUMPY, IPYTHON AND JUPYTER (Walt et al. 2011; Pérez & Granger 2007; Kluyver et al. 2016) and YT (Turk et al. 2011) PYTHON packages. Results in this paper have been derived using the healpy (Zonca et al. 2019) and HEALPix (Gorski et al. 2005) packages.

References

Agertz O., Kravtsov A. V., 2015, *ApJ*, **804**, 18
 Agertz O., Kravtsov A. V., 2016, *ApJ*, **824**, 79
 Agertz O., Kravtsov A. V., Leitner S. N., Gnedin N. Y., 2013, *ApJ*, **770**, 25
 Agertz O., et al., 2021, *MNRAS*, **503**, 5826
 Alves J., Lombardi M., Lada C. J., 2017, *A&A*, **606**, L2
 Applebaum E., Brooks A. M., Quinn T. R., Christensen C. R., 2020, *MNRAS*, **492**, 8
 Applebaum E., Brooks A. M., Christensen C. R., Munshi F., Quinn T. R., Shen S., Tremmel M., 2021, *ApJ*, **906**, 96
 Benincasa S. M., et al., 2020, *MNRAS*, **497**, 3993
 Berkhuijsen E. M., Fletcher A., 2008, *MNRAS*, **390**, L19
 Berkhuijsen E. M., Fletcher A., 2015, *MNRAS*, **448**, 2469

Bianco M., Iliev I. T., Ahn K., Giri S. K., Mao Y., Park H., Shapiro P. R., 2021, *MNRAS*,
 Brook C. B., Stinson G., Gibson B. K., Wadsley J., Quinn T., 2012, *MNRAS*, **424**, 1275
 Buck T., Dutton A. A., Macciò A. V., 2019, *MNRAS*, **486**, 1481
 Buck T., Obreja A., Macciò A. V., Minchev I., Dutton A. A., Ostriker J. P., 2020a, *MNRAS*, **491**, 3461
 Buck T., Pfrommer C., Pakmor R., Grand R. J. J., Springel V., 2020b, *MNRAS*, **497**, 1712
 Buck T., Rybizki J., Buder S., Obreja A., Macciò A. V., Pfrommer C., Steinmetz M., Ness M., 2021, arXiv e-prints, p. [arXiv:2103.03884](https://arxiv.org/abs/2103.03884)
 Burkhart B., Lazarian A., 2012, *ApJ*, **755**, L19
 Christensen C., Quinn T., Governato F., Stilp A., Shen S., Wadsley J., 2012, *MNRAS*, **425**, 3058
 Domínguez-Tenreiro R., Obreja A., Granato G. L., Schurer A., Alpares P., Silva L., Brook C. B., Serna A., 2014, *MNRAS*, **439**, 3868
 Dubey A., et al., 2008, in Pogorelov N. V., Audit E., Zank G. P., eds, *Astronomical Society of the Pacific Conference Series Vol. 385, Numerical Modeling of Space Plasma Flows*. p. 145
 Eckert D., Roncarelli M., Etori S., Molendi S., Vazza F., Gastaldello F., Rossetti M., 2015, *Monthly Notices of the Royal Astronomical Society*, **447**, 2198
 Elmegreen B. G., 2002, *ApJ*, **577**, 206
 Emerick A., Bryan G. L., Mac Low M.-M., 2018, *ApJ*, **865**, L22
 Emerick A., Bryan G. L., Mac Low M.-M., 2019, *MNRAS*, **482**, 1304
 Federrath C., Klessen R. S., 2012, *ApJ*, **761**, 156
 Federrath C., Roman-Duval J., Klessen R. S., Schmidt W., Mac Low M. M., 2010, *A&A*, **512**, A81
 Fryxell B., et al., 2000, *ApJS*, **131**, 273
 Genel S., et al., 2019, *ApJ*, **871**, 21
 Girichidis P., Konstantin L., Whitworth A. P., Klessen R. S., 2014, *ApJ*, **781**, 91
 Girichidis P., et al., 2016, *MNRAS*, **456**, 3432
 Girichidis P., Seifried D., Naab T., Peters T., Walch S., Wünsch R., Glover S. C. O., Klessen R. S., 2018, *MNRAS*, **480**, 3511
 Glover S. C. O., Mac Low M.-M., 2007, *ApJS*, **169**, 239
 Gnedin N. Y., Kravtsov A. V., 2010, *ApJ*, **714**, 287
 Gnedin N. Y., Kravtsov A. V., 2011, *ApJ*, **728**, 88
 Gnedin N. Y., Tassis K., Kravtsov A. V., 2009, *ApJ*, **697**, 55
 Gorski K. M., Hivon E., Banday A. J., Wandelt B. D., Hansen F. K., Reinecke M., Bartelmann M., 2005, *ApJ*, **622**, 759–771
 Governato F., et al., 2010, *Nature*, **463**, 203
 Grand R. J. J., et al., 2017, *MNRAS*, **467**, 179
 Gutcke T. A., Pakmor R., Naab T., Springel V., 2021, *MNRAS*, **501**, 5597
 Haid S., Walch S., Naab T., Seifried D., Mackey J., Gatto A., 2016, *MNRAS*, **460**, 2962
 Hennebelle P., Chabrier G., 2008, *ApJ*, **684**, 395
 Heyer M., Dame T. M., 2015, *ARA&A*, **53**, 583
 Hopkins P. F., Quataert E., Murray N., 2011, *MNRAS*, **417**, 950
 Hopkins P. F., et al., 2018, *MNRAS*, **480**, 800
 Hunter J. D., 2007, *Computing In Science & Engineering*, **9**, 90
 Jones E., Oliphant T., Peterson P., et al., 2001–, SciPy: Open source scientific tools for Python, <http://www.scipy.org/>
 Kainulainen J., Beuther H., Henning T., Plume R., 2009, *A&A*, **508**, L35
 Kakiichi K., Gronke M., 2019, arXiv e-prints, p. [arXiv:1905.02480](https://arxiv.org/abs/1905.02480)
 Kannan R., et al., 2014, *MNRAS*, **437**, 2882
 Kannan R., Vogelsberger M., Stinson G. S., Hennawi J. F., Marinacci F., Springel V., Macciò A. V., 2016, *MNRAS*, **458**, 2516
 Kannan R., Marinacci F., Vogelsberger M., Sales L. V., Torrey P., Springel V., Hernquist L., 2020, *MNRAS*, **499**, 5732
 Keller B. W., Wadsley J. W., Wang L., Kruijssen J. M. D., 2019, *MNRAS*, **482**, 2244
 Kennicutt R. C., Evans N. J., 2012, *ARA&A*, **50**, 531

- Khullar S., Federrath C., Krumholz M. R., Matzner C. D., 2021, [MNRAS](#),
- Kim C.-G., Ostriker E. C., 2015, [ApJ](#), **802**, 99
- Klessen R. S., 2000, [ApJ](#), **535**, 869
- Kluyver T., et al., 2016, in Loizides F., Schmidt B., eds, Positioning and Power in Academic Publishing: Players, Agents and Agendas. pp 87 – 90
- Konstandin L., Girichidis P., Federrath C., Klessen R. S., 2012, [ApJ](#), **761**, 149
- Kreckel K., et al., 2018, [ApJ](#), **863**, L21
- Krumholz M. R., McKee C. F., 2005, [ApJ](#), **630**, 250
- Lancaster L., Ostriker E. C., Kim J.-G., Kim C.-G., 2021a, [ApJ](#), **914**, 89
- Lancaster L., Ostriker E. C., Kim J.-G., Kim C.-G., 2021b, [ApJ](#), **914**, 90
- Leroy A. K., et al., 2013, [ApJ](#), **769**, L12
- Li Y., Klessen R. S., Mac Low M.-M., 2003, [ApJ](#), **592**, 975
- Lupi A., Bovino S., Capelo P. R., Volonteri M., Silk J., 2018, [MNRAS](#), **474**, 2884
- Mao Y., Koda J., Shapiro P. R., Iliev I. T., Mellema G., Park H., Ahn K., Bianco M., 2020, [MNRAS](#), **491**, 1600
- Marinacci F., Sales L. V., Vogelsberger M., Torrey P., Springel V., 2019, [MNRAS](#), **489**, 4233
- Micic M., Glover S. C. O., Federrath C., Klessen R. S., 2012, [MNRAS](#), **421**, 2531
- Munshi F., Brooks A. M., Christensen C., Applebaum E., Holley-Bockelmann K., Quinn T. R., Wadsley J., 2019, [ApJ](#), **874**, 40
- Naab T., Ostriker J. P., 2017, [ARA&A](#), **55**, 59
- Nelson R. P., Langer W. D., 1997, [ApJ](#), **482**, 796
- Nordlund Å. K., Padoan P., 1999, in Franco J., Carraminana A., eds, *Interstellar Turbulence*. p. 218 ([arXiv:astro-ph/9810074](#))
- Obreja A., Macciò A. V., Moster B., Udrescu S. M., Buck T., Kannan R., Dutton A. A., Blank M., 2019, [MNRAS](#), **490**, 1518
- Ostriker E. C., Stone J. M., Gammie C. F., 2001, [ApJ](#), **546**, 980
- Padoan P., Nordlund Å., 2002, [ApJ](#), **576**, 870
- Pérez F., Granger B. E., 2007, [Computing in Science and Engineering](#), **9**, 21
- Pfrommer C., Pakmor R., Schaal K., Simpson C. M., Springel V., 2017, [MNRAS](#), **465**, 4500
- Robertson B. E., Kravtsov A. V., 2008, [ApJ](#), **680**, 1083
- Semenov V. A., Kravtsov A. V., Gnedin N. Y., 2017, [ApJ](#), **845**, 133
- Semenov V. A., Kravtsov A. V., Gnedin N. Y., 2021, *Spatial Decorrelation of Young Stars and Dense Gas as a Probe of the Star Formation-Feedback Cycle in Galaxies* ([arXiv:2103.13406](#))
- Slyz A. D., Devriendt J. E. G., Bryan G., Silk J., 2005, [MNRAS](#), **356**, 737
- Smith M. C., Bryan G. L., Somerville R. S., Hu C.-Y., Teyssier R., Burkhardt B., Hernquist L., 2020, *arXiv e-prints*, [p. arXiv:2009.11309](#)
- Somerville R. S., Davé R., 2015, [ARA&A](#), **53**, 51
- Steinwandel U. P., Moster B. P., Naab T., Hu C.-Y., Walch S., 2020, [MNRAS](#), **495**, 1035
- Stinson G. S., Brook C., Macciò A. V., Wadsley J., Quinn T. R., Couchman H. M. P., 2013, [MNRAS](#), **428**, 129
- Turk M. J., Smith B. D., Oishi J. S., Skory S., Skillman S. W., Abel T., Norman M. L., 2011, [ApJS](#), **192**, 9
- Vazquez-Semadeni E., 1994, [ApJ](#), **423**, 681
- Vogelsberger M., Marinacci F., Torrey P., Puchwein E., 2020, [Nature Reviews Physics](#), **2**, 42
- Wada K., Norman C. A., 2007, [ApJ](#), **660**, 276
- Walch S., et al., 2015, [MNRAS](#), **454**, 246–276
- Walt S. v. d., Colbert S. C., Varoquaux G., 2011, [Computing in Science and Engg.](#), **13**, 22
- Zonca A., Singer L., Lenz D., Reinecke M., Rosset C., Hivon E., Gorski K., 2019, [Journal of Open Source Software](#), **4**, 1298